Shaqour, Ayas; Farzaneh, Hooman; Yoshida, Yuichiro; Hinokuma, Tatsuya

Article

Power control and simulation of a building integrated stand-alone hybrid PV-wind-battery system in Kasuga City, Japan

Energy Reports

Provided in Cooperation with:
Elsevier

Suggested Citation: Shaqour, Ayas; Farzaneh, Hooman; Yoshida, Yuichiro; Hinokuma, Tatsuya (2020) : Power control and simulation of a building integrated stand-alone hybrid PV-wind-battery system in Kasuga City, Japan, Energy Reports, ISSN 2352-4847, Elsevier, Amsterdam, Vol. 6, pp. 1528-1544, https://doi.org/10.1016/j.egyr.2020.06.003

Energy Reports 6 (2020) 1528–1544

Contents lists available at ScienceDirect

Energy Reports

journal homepage: www.elsevier.com/locate/egyr

Research paper

Power control and simulation of a building integrated stand-alone hybrid PV-wind-battery system in Kasuga City, Japan

Ayas Shaqour [a], Hooman Farzaneh [a,b,*], Yuichiro Yoshida [a], Tatsuya Hinokuma [a]

[a] Interdisciplinary Graduate School of Engineering Sciences, Kyushu University, Fukuoka, Japan
[b] Platform of Inter/Transdisciplinary Energy Research, Kyushu University, Fukuoka 819-0395, Japan

ARTICLE INFO

Article history:
Received 18 March 2020
Received in revised form 13 May 2020
Accepted 11 June 2020
Available online xxxx

Keywords:
Building-integrated renewables
Standalone
Hybrid renewables
Solar array
PV
Wind turbine
PI control
P&O
Maximum power tracking
Battery control
Inverter control
Buck converter
MATLAB
Simulink

ABSTRACT

With buildings accounting for high electrical demand and GHG emissions in Japan, enabling higher penetration of hybrid renewable energy systems can significantly reduce their load demand. This paper proposes an efficient power control scheme and design for a hybrid renewable standalone system installed on the roof of a building in Kasuga-City, Japan. The proposed system consists of three PV modules with a total power of (480 W), a wind turbine (400 W), a lead–acid battery (30 Ah), an inverter, and controllers. The main purpose of this research is to implement a well-defined control scheme for standalone Hybrid Renewable Energy Systems (HRES), that has a low level of complexity in terms of Maximum Power Point Tracking (MPPT) with a limited number of components in order to reduce costs and provide high power quality output. The main control layers of the model include the Perturb and Observe (P&O) controller used for MPPT of both the wind turbine and PV systems and a PI controller used to control both the battery charging and inverter of the system. The proposed control scheme also includes two charging modes for the battery when there is no load; Bulk mode for faster charging and Float mode for slower charging to keep the battery fully charged, as its charge decrease with time Dynamic modeling and simulation are accomplished using MATLAB-Simulink™ 9.3, to evaluate the performance and system's dynamics, considering two scenarios of (1) variable weather conditions and (2) different charging modes of battery. The results of the simulation reveal that the proposed system can utilize an efficient battery charging control configuration, eliminating the need for a specific battery converter, providing high output power quality with the Total Harmonic Distortion(THD) below 1% in steady-state, and sustaining output voltage magnitude and frequency under changing system dynamics.

1. Introduction

With the rapid growth in energy demand and rising concerns towards environmental impacts due to the high reliability on fossil fuels, renewable energy generation and clean energy technologies play a vital role in future sustainable power systems (Pérez-Lombard et al., 2008; Höök and Tang, 2013; Ellabban et al., 2014). After the Great East Japan Earthquake, Japan has reduced its dependence on nuclear energy, which accounted for more than 30% of Japan's energy mix, drastically below 2% due to the loss of public trust in nuclear power. While Japan is one of the world's leading energy consumers, its energy self-sufficiency rate is remarkably low, and its level of dependence on imports of fossil fuels from abroad is high, causing energy security challenges for Japan. Fossil fuels currently account for 83.7% of the total energy consumption in Japan, which approaches the level of the oil shock in 1973 (METI/ANRE, 2018). To tackle this challenge, the government of Japan has begun to develop and utilize renewable energy sources to increase its energy self-sufficiency rate and reduce the environmental impacts of the increased use of fossil fuels. The integration of renewable energies in Japan is on the rise, in 2017 renewable energy share of primary energy supply increased by 0.7%, accounting for 8% of the total share (METI/ANRE, 2018; McLellan et al., 2013; Esteban et al., 2018; Farzaneh, 2018).

Buildings accounted for approximately 29% of energy consumption in Japan by 2017 (Akira et al., 2018). Energy consumption in Buildings can be reduced either by increasing building's energy efficiency with improved energy systems (Rocha et al., 2015; Afram et al., 2017; Papantoniou et al., 2015) and thermal efficiency (Gong et al., 2016) or by introducing distributed renewable energy systems and micro-generation systems such as photovoltaic (Athukorala et al., 2015) and Wind turbines (Li et al., 2016; Walker, 2011) to decrease energy demand from the power grid and improve buildings' energy sustainability (Le Guen et al.,

* Correspondence to: Kyushu University, Interdisciplinary Graduate School of Engineering Sciences, 6-1, Kasuga-koen, Kasuga-shi, Fukuoka, 816-8580, Japan.
E-mail address: farzaneh.hooman.961@m.kyushu-u.ac.jp (H. Farzaneh).

https://doi.org/10.1016/j.egyr.2020.06.003

2018; Takatsu and Farzaneh, 2020). Since renewable energies are from the natural environment, they are all-weather dependent, which makes them vulnerable when applying one renewable source to build a stable power system. Using a combination of multiple renewable sources such as solar and wind complement each other, where sunlight is available through the day, and wind energy at night in the winter and summer (Deshmukh and Deshmukh, 2008). The hybridization of variable renewables can allow for smooth, durable, and reliable output to power grids to improve the safety, reliability, and stability of dispatched power, which is cheaper than investing in single renewable technologies (Eleftheriadis and Anagnostopoulou, 2015). HRES as a term is becoming more prevalent under the concept of micro-grids and decentralized/distributed generation (DG), where multiple sources of renewable energies such as (Photovoltaic, Wind turbines, Fuel cells, etc.) are in the same micro-grid, working together with other decentralized non-renewable power generation units in a coordinated manner, designed to suit the demand of a particular area or load (Morais et al., 2010; Farzaneh, 2019b).

Furthermore, when the HRES is connected to a storage system like a battery, the excess energy generated by the solar system or wind turbine can be stored and then utilized during the period when there is no sunshine and wind and electricity is not being generated. Therefore, compared to a single renewable technology, HRES works more efficiently in all operating conditions. On a more general level, hybrid systems can be classified to grid-connected and standalone in terms of connection, and to the type of renewables and non-renewables included as well as the type of storage element used if it exists (Kartite and Cherkaoui, 2019). Emerging smart buildings (Di Piazza et al., 2017; Ma et al., 2016; Kaygusuz et al., 2013) with advanced communication, processing power, and control significantly enable the HRES and micro-grids with high-level demand-load balancing and dispatch optimization (Rouholamini and Mohammadian, 2015; Dulău et al., 2016). To enable such integration, micro-grid modeling of renewable energy systems is widely used to analyze the dynamic behavior of micro-grids under different circumstances while being connected to the power grid (Alzahrani et al., 2017). The optimal design and operation of an HRES in autonomous mode needs a solid understanding of the dynamic nature of the renewable energy sources, and also the technical viability of the system due to adopting a robust control strategy for extracting maximum required power to meet load demand and also to sustain required the State of Charge for the storage element (Valenciaga and Puleston, 2005). The efforts that have been done to address this issue were presented by different scholars who have developed micro-simulation models with a particular focus on the technical level and dynamic analysis of Hybrid systems (Bae and Kwasinski, 2012a). Table 1 shows the recent work being done in the field of dynamic modeling and design of hybrid PV/Wind systems with integrated battery storage.

Kim et al. presented power control strategies for a grid-connected PV, wind, and battery hybrid system, they introduced versatile power transfer and supervisory control for multiple operation modes. They also added a modified hysteresis control for the converter of the battery. Their grid-connected achieved a Total Harmonic Distortion (THD) below 0.35% (Kim et al., 2008a). Gacia et al. introduced and evaluated a neuro-fuzzy inference system energy management system for a grid-connected hybrid PV, wind, battery, and Hydrogen energy (Hydrogen Tank, Electrolyzer, and fuel cell). Their simulation and dynamic analysis showed improved system performance over classical EMS systems, achieving 4.11% THD (García et al., 2014). Although, grid-connected systems can maintain high power quality through sustaining the frequency at the rated level from the power provided from the grid, it is more challenging when it comes to standalone systems.

Caisheng and M. Hashem Nehrir proposed a power management system for a DC linked off-grid hybrid energy system composed of a wind turbine, PV system, and a fuel cell used for energy storage as well as a battery. Their control scheme balances the energy between the different energy sources, the Battery, Load, and Electrolyzer (Wang and Nehrir, 2008). Yoshida and Farzaneh applied the Particle Swarm Optimization (PSO) method to find the optimal configuration of a stand-alone microgrid (PV/wind/battery/diesel) used in providing required electricity for the residential area in Fukuoka (Farzaneh, 2019a). Farzaneh conducted the techno-economic analysis of a hydrogen-based HRES, consisting of a biomass supercritical gasifier and a solar water electrolyzer, which are linked to the PV panel and fuel cell. The proposed HRES was used to provide electricity, heat, hydrogen, and water to the small community in Fukushima (Yoshida and Farzaneh, 2020). M. Kalantar and S.M. Mousavi G. introduced a dynamic simulation of a standalone HRES power system, combining a wind turbine (195 kW), solar array (85 kW), battery storage (2.14 kAh) and a micro-turbine (230 kW). They also compared fuzzy logic control with a proposed adaptive controller to implement maximum power tracking for the wind turbine (Kalantar and Mousavi, 2010). Belabbas et al. simulated and presented a standalone hybrid power system composed of Photovoltaic panels as the main renewable energy source, a Diesel Generator for energy back up and a Battery Storage. They proposed a hierarchal power management scheme, where the first layer uses fuzzy logic control to control the voltage and frequency at the point of common coupling with a clamping bridge circuit to regulate the DC bus voltage, it also uses fuzzy logic control to extract maximum power point from the PV array. The Second layer of their proposed control controls the power flow from different sources to ensure optimized power flow to the load. Their proposed system had a Total Harmonic Distortion(THD) of 5.9% (Belabbas et al., 2019). Kumar et al. discussed the design and analysis of a standalone hybrid energy system combining wind and PV power. They proposed a Cuk-SEPIC converter to eliminate the need of a harmonic filter, where the output of their inverter achieved 5.39% THD. They also proposed the use of incremental conductance with integral control to extract maximum power from the wind turbine and Perturb and Observe to obtain maximum power from the PV array (Kumar et al., 2017). Also, while fuzzy logic and neural networks can add a high level of control, they are more complex and system-specific compared to other more general algorithms that are less complex and require less information and sensors.

In order to develop a low cost highly efficient stand-alone hybrid systems, that can be integrated with buildings or rural areas, a low-complex MPPT, high power quality output system for achieving THD below 1% in steady state, without the need of a battery specific converter to control the charging and discharging modes has yet to be developed. To this aim, this research focuses on introducing a standalone residential HRES, in a range of few kilowatts, that can reach this goal. The proposed standalone HRES in this research consists of a wind turbine, PV array, and battery storage, as shown in Fig. 1. The control scheme has three layers of control, to extract maximum power from both the wind and PV array, control the DC bus voltage to control the charging of the battery and control the inverter output voltage and frequency to meet the AC load requirements. Compared to the previously discussed literature, the proposed system uses both DC–DC converters of PV and Wind for maximum power tracking as well as control the battery charging and operation, eliminating the need for a specific battery charger circuit, thus reducing costs. The proposed control model also provides detailed simulation and analysis of the inverter control to improve power quality and how it is used in the battery control scheme. Finally, the proposed

Table 1
Types of design and control of standalone and grid-connected hybrid systems.

System configuration	Control techniques	Control elements	Software	Reference
Off-Grid Hybrid PV/Wind/Battery	Incremental conductance and PI control.	Boost Converter, Inverter.	MATLAB-Simulink	Sikder and Pal (2019)
Off-Grid Hybrid PV/Wind/Battery	PI and Fuzzy Logic Control.	Bidirectional Buck-Boost Converter, Inverter.	MATLAB-Simulink	Das and Akella (2018)
Off-Grid Hybrid PV/Wind/Battery	P&O, Sliding Mode Control and PI Control.	Buck Converter, Boost Converter.	PSIM Tool	Akram et al. (2017)
On/Off Grid Hybrid PV/Wind/Battery	P&O, Sliding Mode Control and PI Control.	Boost Converter, Boost-Buck Converter, Inverter.	MATLAB-Simulink	Sassi et al. (2017)
On-Grid Hybrid PV/Wind/Battery	PI Control	Bidirectional buck-boost converter, full-bridge bidirectional converter, transformer-coupled boost dual-half-bridge bidirectional converter.	MATLAB-Simulink	Mangu et al. (2016)
Off-Grid Hybrid PV/Wind/Battery	Incremental conductance and PID control.	MI Ćuk Converter Among, Inverter.	MATLAB-Simulink/ LabVIEW	Bae and Kwasinski (2012b)
Off-Grid Hybrid PV/Wind/Battery	PID Control	Buck Converter	MATLAB-Simulink	Husain (2013)
On/Off-grid Hybrid PV/Wind/Battery	PI Control	Buck Converter, Inverter.	Tek measurement software	Dali et al. (2010)

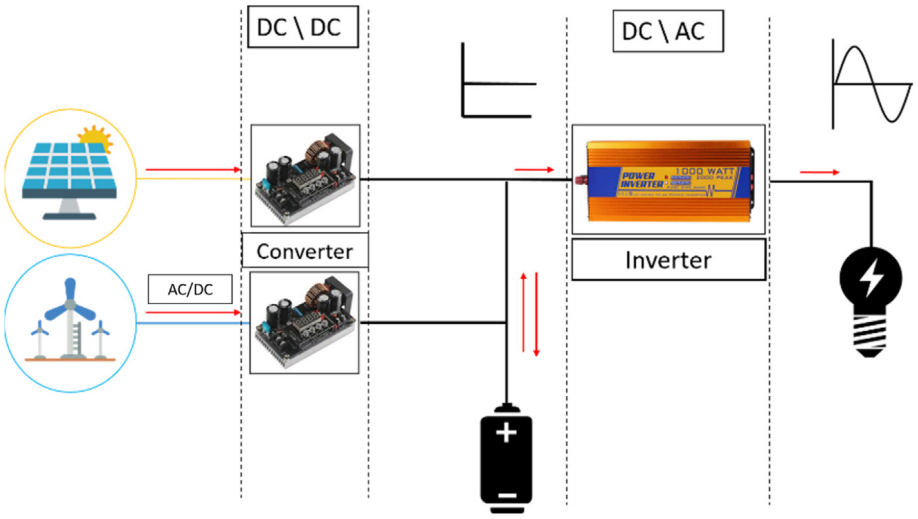

Fig. 1. Standalone-PV/Wind/Battery HRES.

filter designs meet the output voltage allowed harmonic limits according to standards, improving the power quality.

This paper is organized as follows: Section 2 presents the control strategies for the maximum power point tracking of the PV array using P&O, the Battery Charge control, the Inverter control, and the Buck Converter Control. Section 3 discusses the modeling of HRES components. Section 4 presents a case study. Section 5 presents the MATLAB simulation. Section 6 presents the simulation results and discussion. Section 7 concludes the paper.

2. HRES power control strategies

A simple HRES usually consists of a PV system, a wind turbine, and mainly a battery or energy storage element. DC–DC converters are used to control the DC voltage, and an inverter is used to convert the voltage from DC to AC as well as control the output voltage to be at the required level under different circuit conditions. The major objectives of the control system in an HRES are to track the maximum power under different environmental conditions, to control the battery charging modes, and to keep the output voltage and frequency under the required levels. In the following section, the main three control strategies which are used in a standalone HRES will be discussed.

2.1. PV maximum power tracking

Fig. 2 Shows the Power–Voltage curve of a PV system under varying weather conditions. It can be observed that under various radiation conditions and ambient temperatures, the solar PV presents different maximum power points. The maximum power point occurs at the point where the PV voltage and current ($V * I$) achieve the highest value, it is the point where the characteristic impedance of the PV array matches the load resistance. In order to track this maximum point, several techniques are used in practice and the literature, each varying in the complexity of implementation, cost, efficiency, and tracking speed (Saravanan and Ramesh Babu, 2016; Jordehi, 2016). While there exist many highly efficient techniques like Fuzzy logic and Neural networks, they are costly and complicated, whereas, Perturb and Observe (P&O), and incremental conductance are two of the more popular techniques currently in use, since they are direct methods that can work under any meteorological condition and do not need temperature, nor irradiance sensing (Bendib et al., 2015); where using such sensors are not advised and costly (Femia et al., 2017). Therefore, they do not need any pre-knowledge of the system data; hence they are compatible with any type of HRES (Sera et al., 2013; De Brito et al., 2013).

P&O is a blind hill-climbing algorithm, as shown in Fig. 3, that attempts to find the local or global maximum of a system.

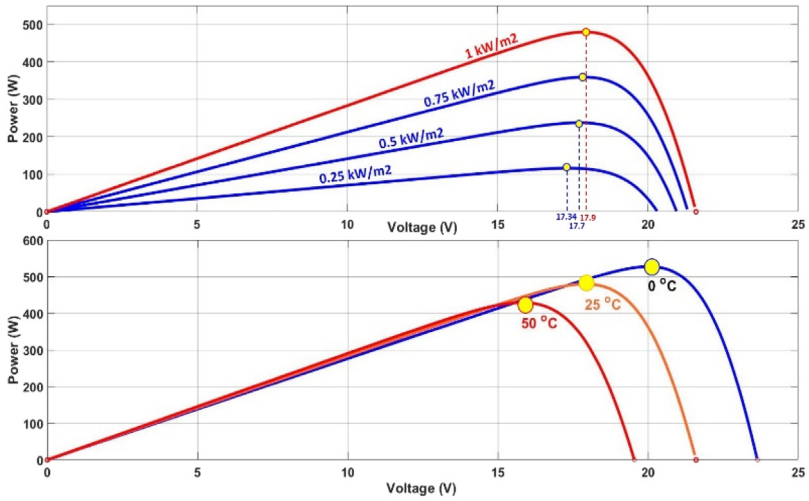

Fig. 2. PV power and voltage output under different irradiances and temperatures.

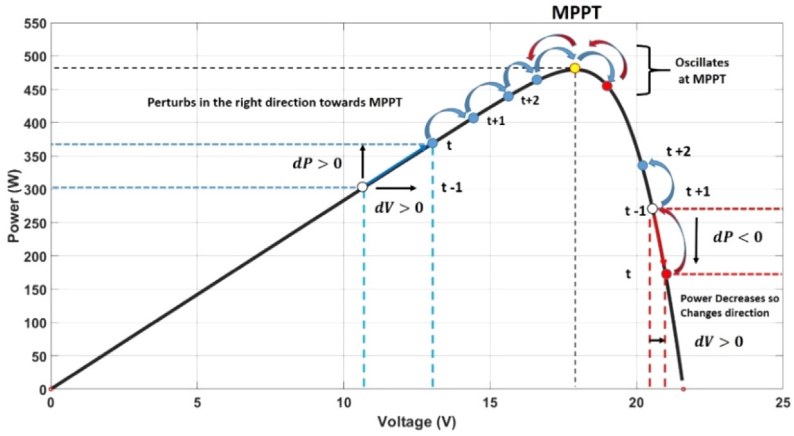

Fig. 3. PV power–voltage characteristic at 1 kW/m^2 irradiance showing P&O operation.

Based on P&O, the control system perturbs the working point (at the time $(t-1)$) on the P–V curve of the PV system, then observes the change in power output (dP), if, after the perturbation, $dP > 0$, it means that the change was in the direction of the maximum power point. Hence, the algorithm keeps perturbing in that direction until it reaches the maximum power point. If the algorithm perturbs in a direction that gives $dP < 0$, it moves towards the opposite direction of the MPPT, so it perturbs in the opposite direction. When the MPPT is reached, P&O oscillates around it, making power loss according to the perturbation step size (De Brito et al., 2013). From a technical point of view, The P&O algorithm starts by reading the values for voltage and current output from the PV array, then changing the duty cycle of the DC–DC converter with a fixed step and finally calculating the change in power and voltage caused by the difference in duty cycle. If the output power remained constant, it means that the controller has reached the maximum power point, so it does not change the duty cycle for that iteration. Otherwise, it decides to move the working point of the PV system in the direction at which output power increases.

Fig. 4 represents the detailed algorithm used in the Perturb and Observe PV maximum power tracking controller.

2.2. Battery charge control

Battery charge control is of vital importance to standalone HRES systems. The battery's State of Charge (SOC) indicates how much capacity the battery has in order to ensure the battery's safety, lifetime as well as good performance. The depth of discharge (DOD) of a battery indicates how much capacity is used per charging cycle. These two modes of battery charging are as follows:

- Float charging: This mode aims at giving the battery just enough small amount of current to keep it at the required SOC and reduces the voltage to lower levels.
- Charging voltage/bulk charging: This mode aims at giving the battery the required voltage level to quickly charge the battery at the maximum safe current until its voltage is brought up to nearly 85% of the full charge level.

Fig. 5 shows the proposed battery's charging control method, to select between bulk charging and float charging voltage. When the SOC is above 85%, the battery controller will apply a float voltage to the battery, which is used as a reference voltage for the PID controller. When the SOC is between 15% and 85%, the bulk charging voltage will be applied to the battery. The DC bus bar voltage which is the voltage input to the battery is compared to the reference voltage and the error is fed to a PI controller which changes the duty cycle of the DC–DC converter connected to both the wind turbine and PV array, to reach the required reference voltage level. Fig. 6 shows the control flowchart for the battery charging; whenever there is a load connected, the control system prioritizes maximum power tracking. If the battery's charge drops

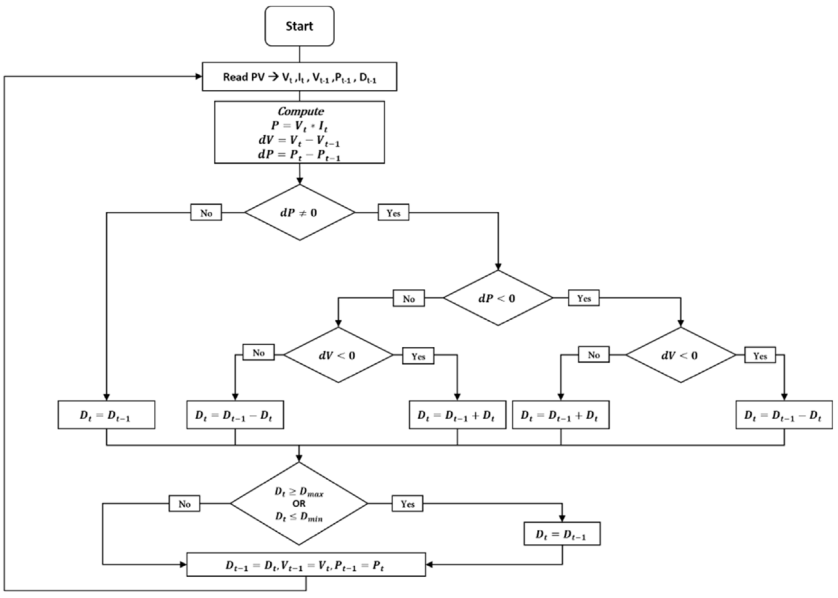

Fig. 4. Perturb and observe PV algorithm.

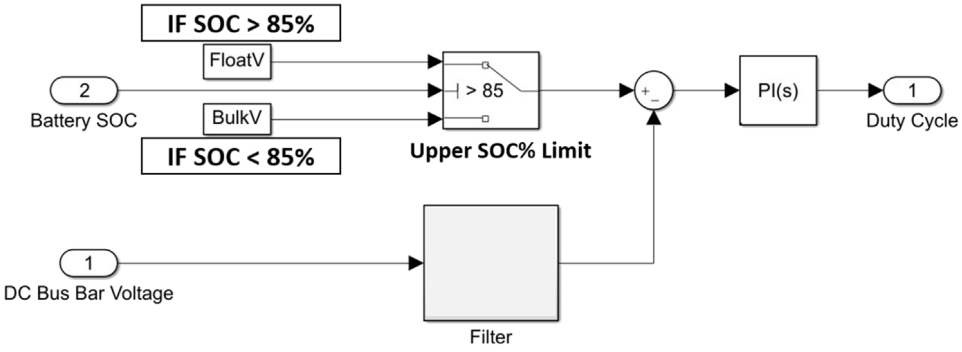

Fig. 5. Battery charge control method.

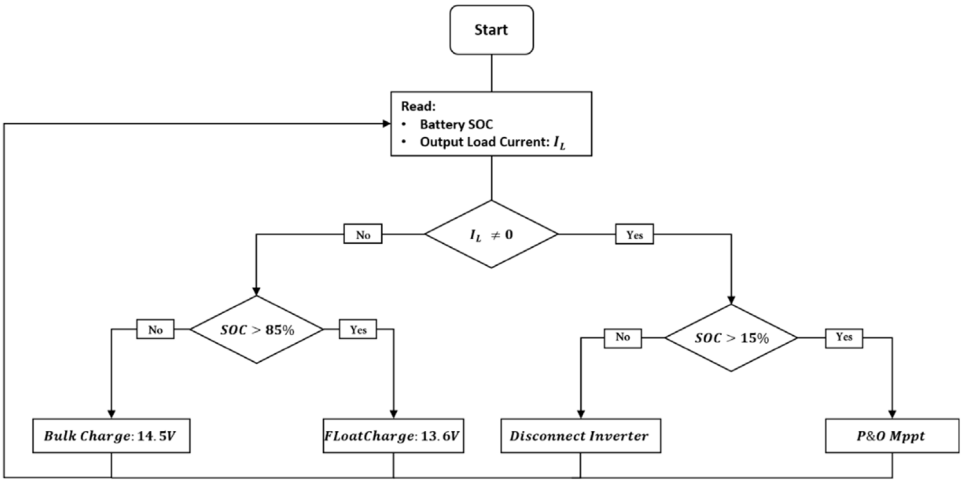

Fig. 6. Battery charge control algorithm.

below 15% of its SOC, the inverter disconnects the load, ensuring the battery's safety. When there is no load connected, the controller prioritizes the DC bus bar's voltage control of the DC–DC converters, ensuring the correct charging mode voltage. For our system the Bulk Charging Voltage has been set to 14.5 V and the Float Charging Voltage to 13.6 V as seen in Fig. 6, this depends on the battery manufacturer recommendation, where these voltages

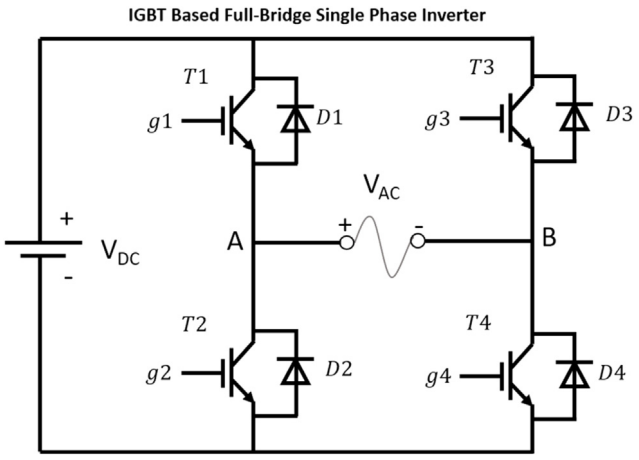

Fig. 7. IGBT based full bridge phase inverter.

resemble the reference voltage for the PI Controller to keep the charging voltage in the correct range.

2.3. Output voltage and frequency control

In order to meet the output voltage and frequency at the required standard values, a control system would be needed to control the inverter of the standalone HRES system, where under changing environmental conditions as well as battery and circuit dynamics, the voltage level input to the inverter is continuously fluctuating, and the output signal is kept stable at the required voltage and frequency as well as standard system harmonic limits. Fig. 7 shows an Insulated-Gate Bipolar Transistor (IGBT) Single-Phase full-bridge inverter consisting of 4 pairs of diodes and transistors. By controlling the switching signals at the gates ($g1, g2, g3, g4$) of the four transistors both output voltage and frequency of the inverter are modulated. A pulse width modulation generator generates the four control signals in a designed sequence and frequency, taking a sine wave as an input, where the frequency of the sine wave and it's amplitude "called the modulation index" determines the output AC signal's frequency and voltage level. As it is depicted in Fig. 8, the PI controller used in the inverter reads the real mean square (RMS) output voltage and compares it to a reference value to modulate the sine wave input to the inverter's PWM generator, and the output voltage to the required level (Bhende et al., 2011; Tan, 2020). As previously discussed, when the battery SOC is below 15%, the four control signals are all set to zero, turning off all the transistors and cutting the inverter's output.

2.4. (DC–DC) buck converter control

In renewable power systems such as PV and Wind, DC–DC converters are used as impedance matching systems, in order to achieve maximum power point tracking (Haroun et al., 2015), They can be used to track the maximum power point of the system, by controlling their duty cycle, thus moving the working point on the I–V curve. Fig. 9 shows the working design of a Buck converter as one of the DC–DC power converters, which is used to step down the voltage level. By switching ON and OFF the circuit at high frequency, the output voltage can be controlled and dropped to the required level. In the ON state, the current increases, inducing a voltage drop across the inductor, hence, decreasing the output voltage. When the circuit is open (OFF), the inductor acts as a current source, releasing its stored energy, if the switch is closed before the stored energy depletes, the output voltage will be continuous. The ON–OFF switching decreases the average output voltage and increases the average current in the circuit, preserving the power delivered to the load. The average output voltage can be calculated using the following formula (Mohan et al., 2003):

$$V_o = \frac{1}{T_s}\int_0^{T_s} v_o\,(t)\,dt = \frac{1}{T_s}\left(\int_0^{t_{on}} v_o\,(t)\,dt + \int_{t_{on}}^{T_s} 0\,dt\right) = \frac{t_{on}}{T_s}V_d = DV_d \tag{1}$$

V_o is the average output voltage of the buck converter, V_d is the Diode voltage, which is the input voltage to the converter. T_s is the switching time ($t_{on} + t_{off}$), t_{on} is the time the circuit is connected (switch is closed). D is the duty ratio, which represents the percentage of the period where the circuit was ON, the higher the value D is, the less the input voltage is stepped down. The diode, which is shown in Fig. 9, allows the inductor current to flow to the load when the switch is open and is reverse biased when the switch is ON. The capacitor smooths the output voltage since it varies between its peak value and zero. The low pass filter filters the harmonics and its corner frequency f_c is usually much lower than the switching frequency of the buck converter to eliminate the ripples caused by it (Mohan et al., 2003).

3. HRES's main components modeling

3.1. Photovoltaic panel

A photovoltaic PV cell is a semiconductor-based device that converts light energy into electricity under the photovoltaic effect. Fig. 10 represents the single-diode five parameters model which is used to represent the characteristics and behavior of a solar module, taking into account the energy losses; a series resistance (R_s) representing the energy loss the current faces through the body of the cell, the contacts' resistance and the metal electrodes' resistance and shunt resistance (R_{sh}) representing the leakage-current (Et-torabi et al., 2017).

In order to draw the (I–V) curve of our PV system, the following equations are used (Et-torabi et al., 2017; Barukčić et al., 2014):

$$I = I_{ph} - I_d - I_{Rsh} \tag{2}$$

Eq. (2) is based on a simple Kirchhoff's current law (KCL). Where I is the output current of the cell, I_{ph} is the photocurrent produced by the cell, I_d is the Diode current and I_{Rsh} is the leakage current going through the Shunt Resistance (R_{sh}). The Current of the diode I_d which depicts the recombination losses in the PV module is expressed as follows:

$$I_d = I_0 * \left[\exp\left[\frac{V_d}{V_T}\right] - 1\right] \tag{3}$$

I_0 is the diode saturation current, V_d is the voltage across the diode and V_T is calculated as follows (Et-torabi et al., 2017; Barukčić et al., 2014):

$$V_T = \frac{KT}{q} * A * N_s \tag{4}$$

K is the Boltzmann constant (1.3806×10^{-23} m^2 kg s^{-2} K^{-1}), T is the temperature in Kelvin, q is the electron charge ($1.6022 * 10^{-19}$ C), A is the diode ideality factor and N_s is the number of cells connected in series. Finally, we can calculate I_{Rsh} *and* V_d using simple circuit analysis, the following expressions are reached (Et-torabi et al., 2017; Barukčić et al., 2014):

$$V_d = V + I * R_s \tag{5}$$

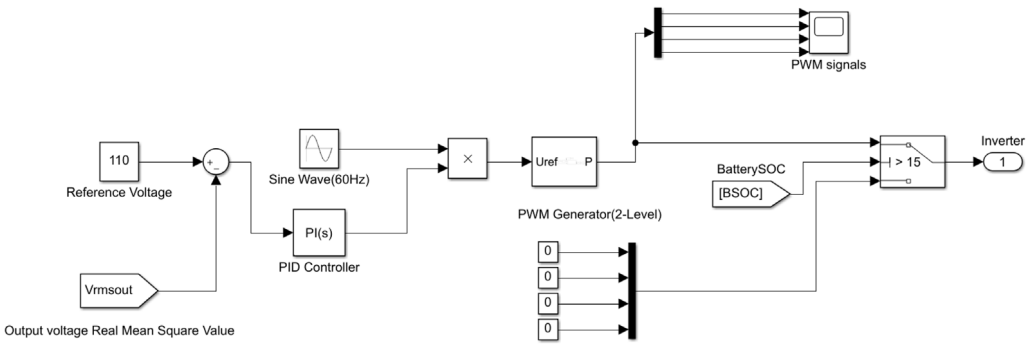

Fig. 8. Inverter's control method.

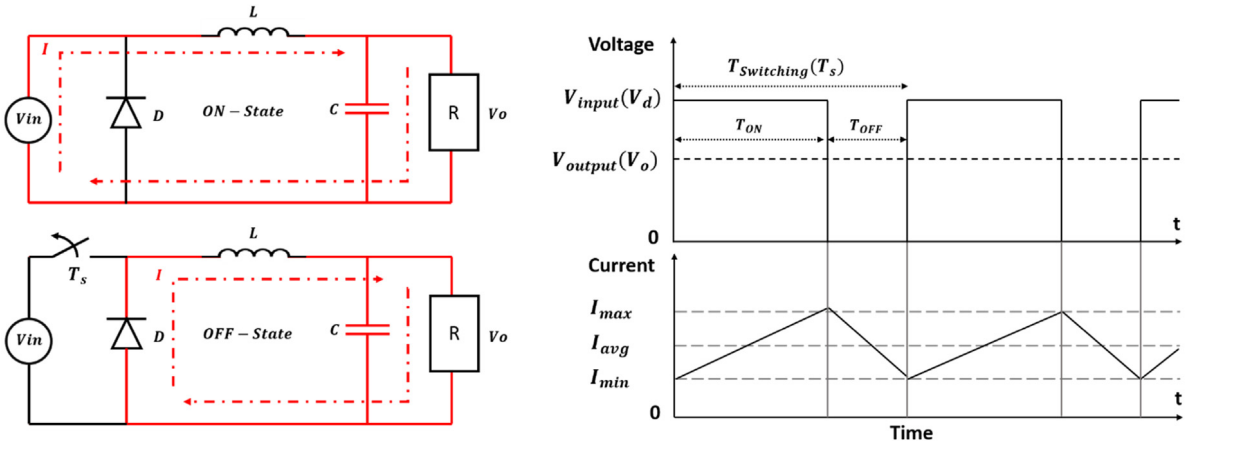

Fig. 9. Buck converter circuit and characteristic.

$$I_{sh} = \frac{I * R_s + V}{R_{sh}} \tag{6}$$

V and I are the output voltage and current of the model respectively, R_s is the series resistance and R_{sh} is the shunt resistance. To calculate the five unknowns (I_{ph}, I_0, R_s, $R_{sh,}$ and A), we have to derive five equations based on the parameters provided by the datasheet (I_{SC}, V_{OC}, I_{mpp}, V_{mpp}, K_I, K_v, and N_s). Using the three points (V_{mpp}, I_{mpp}), (V_{OC},0) and (0, I_{sc}) and different mathematical manipulations, the five equations are obtained, then optimization techniques are used to find and estimate the five parameters (De Soto et al., 2006; Shongwe and Hanif, 2015).

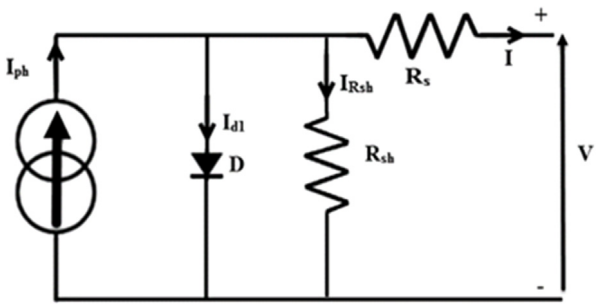

Fig. 10. Single diode PV model.

3.2. Wind power system

A wind power system is composed of three stages; the aerodynamic stage is where kinetic energy in the air is converted to mechanical rotational energy, the mechanical stage where a wind turbine connected to a gearbox to control the torque–speed that will be input to the generator, where mechanical energy is transformed into electrical three-phase waves (Fig. 11). At the third stage, the "Electrical stage", the 3-phase electrical signal is controlled and transformed with converters and inverters to different voltage levels and types (Martinello et al., 2016).

The relationship between wind energy and wind speed in a wind turbine can be expressed as (Hwas and Katebi, 2012; Heier and Waddington, 1998):

$$P_{wt} = 0.5\rho A v 3 C_p(\beta, \lambda) \tag{7}$$

The maximum power (P_{wt}) that can be extracted from the wind turbine is represented in Eq. (7). ρ is Air density kg/m^3, A is the area swept by the turbine in m^2 and v is the wind speed m/s. C_p

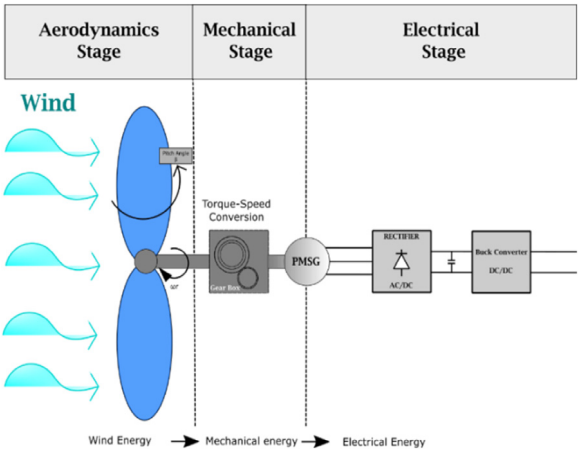

Fig. 11. Wind turbine modeling stages.

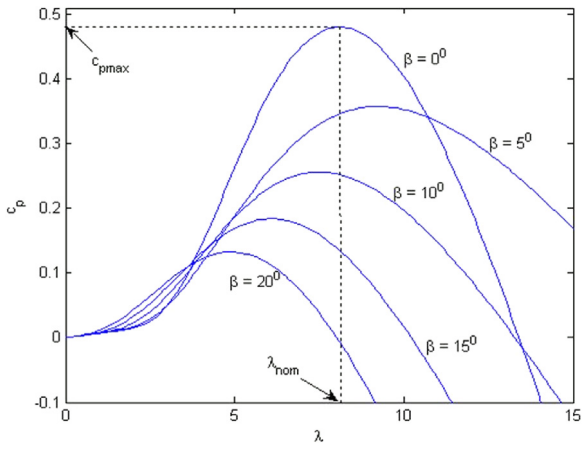

Fig. 12. Wind turbine power coefficient vs. tip speed ratio λ for different pitch angles β.

is called the power coefficient, introduced to represent the Betz limit (maximum 59%), where this power limitation is a function of the tip speed ratio λ and the pitch angle β as can be seen in Fig. 12.

$$C_p = 0.5176\left(\frac{116}{\lambda_i} - 0.4\beta - 5\right)e^{\frac{-21}{\lambda_i}} + 0.0068\lambda \tag{8}$$

C_p can be calculated using Eq. (8), where it is highly non-linear and depends on the pitch angle, wind speed, and the turbine's rotation speed. To calculate C_p, the value of λ_i should be calculated using the following expression (Hwas and Katebi, 2012; Heier and Waddington, 1998):

$$\frac{1}{\lambda_i} = \frac{1}{\lambda + 0.08\beta} - \frac{0.035}{\beta^3 + 1} \tag{9}$$

$$\lambda = \frac{\omega_{wt} R}{v} \tag{10}$$

where λ is the tip speed ratio, which is the ratio between the tip speed and the wind speed v (m/s). The tip speed is calculated by multiplying the turbine rotor speed ω_{wt} (rad/s) by the blade radius R (m). Observing the relationship between C_p and λ for different Pitch angles in Fig. 12, the maximum C_p is 0.48 found at $\beta = 0^o$ and $\lambda = 8.1$. This λ is called the nominal.

3.2.1. Permanent magnet synchronous generator (PSMG)

The PMSG having a permanent magnet raises its efficiency compared to the induction generator that needs excitation with extra energy supply. The voltage and current equations belonging to PMSG are shown below (Ko, 2014; Ackermann, 2005; Krause et al., 2002):

$$\frac{d}{dt}i_d = \frac{1}{L_d}v_d - \frac{R}{L_d}i_d + \frac{L_q}{L_d}pi_q\omega_m \tag{11}$$

$$\frac{d}{dt}i_q = \frac{1}{L_q}v_q - \frac{R}{L_q}i_q - \frac{L_q}{L_q}pi_d\omega_m - \frac{\lambda p\omega_m}{L_q} \tag{12}$$

$$L_d = L_q = \frac{L_{ab}}{2} \tag{13}$$

$$P_s = v_d i_d + v_q i_q, \qquad Q_s = v_d i_q - v_q i_d \tag{14}$$

The subscripts d *and* q represent the direct and quadrature axis components respectively, s indicates the stator, ω_m is the angular velocity of the rotor, λ is the magnitude of the flux caused by the permanent magnet of the rotor in the stator phases, ρ is the number of pole pairs. v *and* i represent the voltage and current and R the resistance of the stator. L_d *and* L_q are the q and d axis inductances and do not vary for round rotors where they can be found using Eq. (13), where L_{ab} is the phase to phase inductance. The active and reactive electrical power of the stator can be found using Eq. (14). The torque expression of PMSG is given below (Krause et al., 2002):

$$T_e = 1.5\rho[\lambda i_q + (L_d - L_q)i_d i_q) \tag{15}$$

And the Relation between the torque and rotor angular velocity is (Krause et al., 2002):

$$\frac{d}{dt}\omega_m = \frac{1}{J}(T_e - T_f - F\omega_m - T_m) \tag{16}$$

$$\frac{d\theta}{dt} = \omega_m \tag{17}$$

where J is the combined inertia of the rotor load, F is the combined viscous friction of rotor and load, θ is the angular position, T_m is the shaft mechanical torque, T_f is the shaft static friction torque and ω_m is the angular velocity of the rotor(mechanical speed).

3.2.2. Rectifier

A three-phase uncontrolled diode rectifier is used to convert the three-phase AC output of the wind turbine into DC. The output voltage of the rectifier can be described by the following equations (Hart Danial, 2010):

$$v_0(t) = V_0 + \sum_{n=6,12,18..}^{\infty} V_n \cos(n\omega_o t + \pi) \tag{18}$$

where the average or dc voltage V_0 *is*:

$$V_0 = \frac{3V_{m,L-L}}{\pi} = 0.955\ V_{m,L-L} \tag{19}$$

And V_n which carries the amplitudes of the voltage terms is equal to:

$$V_n = \frac{6V_{m,L-L}}{\pi(n^2-1)} \quad n = 6, 12, 18\ldots \tag{20}$$

where v_0 is the output voltage of the rectifier, $V_{m.L-L}$ is the line to line peak voltage of the wind turbine output, which equals $\sqrt{2}V_{L-L,rms}$. The harmonics seen from Eq. (20) are of order $6k + 1, k = 1, 2, 3\ldots$ where this makes it easy for filters to be used to eliminate the low amplitude high-frequency components (Hart Danial, 2010).

3.3. Battery storage

The battery's dynamic charge and discharge voltage E_{Batt} can be represented by Fig. 13 and the following equations (Tremblay and Dessaint, 2009):

Discharge Model ($i_l > 0$):

$$E_{Discharge} = f_1(i_t, i_l, i, Exp) = E_0 - K.\frac{Q}{Q - i_t}.i_l - K.\frac{Q}{Q - i_t}.i_t + Laplace^{-1}\left(\frac{Exp(s)}{Sel(s)}.0\right) \tag{21}$$

Charge Model ($i_l < 0$):

$$E_{charge} = f_2(i_t, i_l, i, Exp) = E_0 - K.\frac{Q}{i_l + 0.1Q}.i_l - K.\frac{Q}{Q - i_t}.i_t + Laplace^{-1}\left(\frac{Exp(s)}{Sel(s)}.\frac{1}{s}\right) \tag{22}$$

where E_o *is* constant voltage (V), $Exp(s)$ is the exponential zone dynamics (V), $Sel(s)$ represents the battery mode selection, 0 for discharging, and 1 for charging, K is the polarization resistance

Table 2
Solar panel parameters.

Parameters	Value
Rated power	160 W
Maximum/Peak voltage	17.9 V
Open Circuit voltage	21.6 V
Maximum/Peak current	8.94 A
Short-circuit current	9.47 A
Current temperature coefficient	(0.1 ± 0.01) %/°C
Voltage temperature coefficient	(0.38 ± 0.01) %/°C
Number of cells Ns	36
Temperature range	−40 °C to +80 °C

Table 3
Wind turbine parameters.

Parameters	Value
Rated power	400 W
Rated voltage	12 V
Start-up wind speed	2.5 m/s
Rated wind speed	10.5 m/s
Maximum wind speed	35 m/s
Rated rotation speed	800 r/m
Fan blade quantity	3
Rotor blades diameter	1.2 m

Table 4
Battery parameters (V30-800 Deep Cycle, AGM[a]).

Parameters	Value
Type	Lead acid
Fully charge voltage	14 V
20Hr capacity	30 AH
RC (min)	55
CCA	280
Charging current	2 A–10 A
Charging voltage	14.4–14.9 V
Float voltage	13.5–13.8 V

[a]Absorbent Glass Mat.

in ohms or the polarization constant in V/Ah. i_l is the low-frequency current dynamics (A), and i is the battery current (A). i_t *and* Q refer to the extracted capacity and maximum capacity of the battery, respectively, both in (Ah). And finally, the following expression is used:

$$\frac{Exp\,(s)}{Sel\,(s)} = \frac{A}{\frac{1}{B*i(t)}.s+1} \tag{23}$$

A represents the exponential voltage (V), and B is the exponential capacity (Ah^{-1}). It should be noted that this model does not take into account the Peukert effect, where the capacity of the battery does not change according to the discharge current amplitude. Also, the model's parameters are deduced from the discharging characteristics and are the same for charging (Tremblay and Dessaint, 2009).

4. Case study

To verify the proposed control scheme, a case study of an HRES installed on the roof of a building in Kasuga-City, Fukuoka prefecture, Japan is introduced in this research. The target system consists of three PV modules with a total power of (480 W), a wind turbine (400 W), a lead–acid battery (30 Ah), an inverter, and controllers. Fig. 14 shows the system's components, and Fig. 15 shows the wind turbine's power characteristics. The technical specifications of the proposed system are reported in Tables 2–4.

Table 5
Battery charge controller parameters.

Parameters	Value
Float voltage set point	13.6 V
Buck voltage set point	14.5 V
DC–DC charge controller	**Discrete-time-PI based**
Proportional (p)	5
Integral (I)	150
Anti-windup gain	1
Control action upper limit	1
Control action lower limit	0
Sample time	Inherited
Time constant voltage filter:	0.0001

5. HRES's MATLAB simulation model

The MATLAB simulation model of the proposed HRES system and control scheme is shown in Fig. 16. The details of each block are discussed as follows:

The PV block consists of three PV modules connected in series, each having a rated power of 160 watts. The detailed I–V curve and power curve calculated by the model is shown in Fig. 17. The output of the PV system is connected to a 2200 μF DC link capacitor.

The wind turbine's speed–power curve can be seen in Fig. 18, where the values are in "per unit", in relevance to both the nominal generator speed and mechanical power. A saturation block is used to simulate the maximum speed the turbine can tolerate, and a gain is used to convert the per unit mechanical torque to its real value. A 2200 μF DC link capacitor is connected to the output. First the wind speed, pitch angle, and generator speed are fed to the wind turbine block where the power is calculated, and the per-unit torque is output. The per-unit torque is converted to the actual torque by multiplying it with the base torque, which is calculated in accordance with the rated speed and power of the wind turbine. The estimated torque is fed to the PMSG, and the three-phase voltages are generated. The rectifier converts the three-phase AC voltages into DC. It should be noted that the output generator speed is fed back into the wind turbine block after it is converted to its "Per Unit" value. It is done by dividing its value by the rated rotor speed, which is about 83.77 rad/s (800 rpm).

An Absorbed glass mat (AGM), Lead–acid battery with 30 Ah of capacity is utilized in the proposed system design. Fig. 19 shows the model's output battery discharge characteristics for different discharge currents.

The proposed model utilizes an IGBT Buck converter for each of the PV and Wind turbine systems. It is modeled by an IGBT/diode pairs PWM signal controlled, followed by an inductor, a free-wheeling diode, and a capacitor. The freewheeling diode prevents any currents from entering from another source. Fig. 20 shows the proposed control scheme. The upper part is the P&O algorithm with its initial D, D max, D min and delta D set to 0.7, 0.95, 0.25 and 10^{-5} respectively, where D is the duty cycle. Both PWM generators are set to 30 000 samples per second and a sampling time of 5 μs. The lower part of Fig. 20 represents the battery charge controller with the parameters shown in Table 5. The bulk Charge voltage is set to 14.5 V and the Float charge voltage to 13.5 Volts as per manufacturer's recommendation for the battery (13.5–13.8 V) for Float and (14.4–14.9 V) for Bulk. The model decides the operating condition by reading the output current of the inverter's filter, if it exceeds 0.01A then it is assumed to be connected and works in the MPPT mode, else it works in the Battery Charging mode.

The input of the inverter is connected to two 6600 μF capacitors both used to sustain the DC link's voltage fluctuations

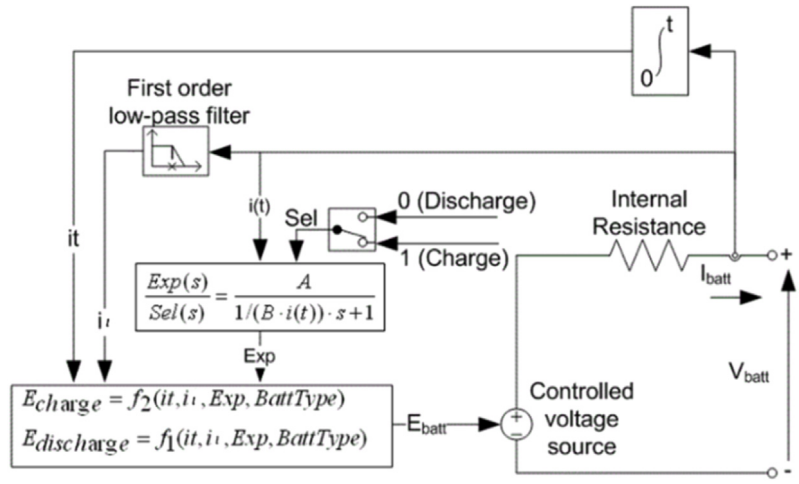

Fig. 13. Battery model.

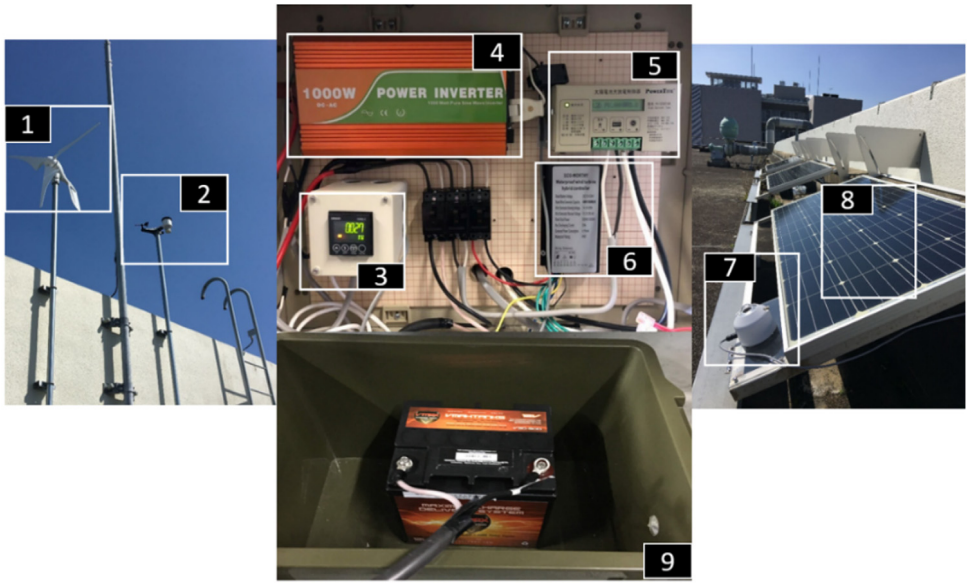

Fig. 14. (1) Wind turbine, (2) Weather measurement station, (3) Data logger, (4) Inverter, (5) PV DC converter and controller,(6) Wind DC converter and controller, (7) Pyranometer, (8) PV module, (9) Battery.

and harmonics caused by the ON/OFF switching of the buck converters as well as the changing dynamics of the system. An IGBT based single-phase full-bridge inverter is connected to an LC filter and Linear Transformer to filter the inverter's harmonics and step up the AC Voltage to the required 110 Voltage.

The LC filter is widely used on the output of PWM inverters when the target control is the Voltage (Kim and Sul, 2011), where it is used to filter out unwanted harmonics and to keeping the Total Harmonic Distortion of the system under the maximum allowed value. The filter attenuates unwanted ripple waves that are induced by the inverter's switching (Kim et al., 2008b). It is a second-order filter that has a simple configuration; hence, it is easy to design and works well with no problems. It has to be also noted that the design of the filter needs a high enough capacitance to improve voltage quality and a high enough inductance to achieve the target cut-off frequency (El Wahid Hamza et al., 2015). The cutoff frequency is described by (T.I. Incorporated, 2000; Dahono et al., 1995):

$$f_c = \frac{\omega_c}{2\pi} = \frac{1}{2\pi . \sqrt{L_f . C_f}} \tag{24}$$

f_c is the cutoff frequency of the filter in Hz, ω_c is the angular cutoff frequency in rad/s, L_f is the LC filter inductor and C_f is the filter's capacitor. It is recommended in Dahono et al. (1995) to design the cutoff frequency according to the following relation:

$$\omega_c = \frac{1}{\sqrt{L_f . C_f}} \leq \frac{\omega_{sw}}{10} \tag{25}$$

where ω_{sw} is the switching frequency of the inverter, with f_{sw} being 1620 Hz. The proposed filter has been designed at a cutoff frequency of 67.9 Hz with an inductance of $L_f = 500\ \mu H$ *and a capacitance* $C_f = 2200 * 5\ \mu F$. A 1000 W, 60 Hz single-phase linear transformer was used in the proposed model with (Winding 1) rated at 12 V and (Winding 2) rated at 110 V.

6. HRES simulation results and discussion

To verify the proposed control scheme and model's performance under various working conditions and show the state of the different voltages, currents, power states, and harmonics of the system's components, two different scenarios have been implemented. The first showing the system's dynamics and control

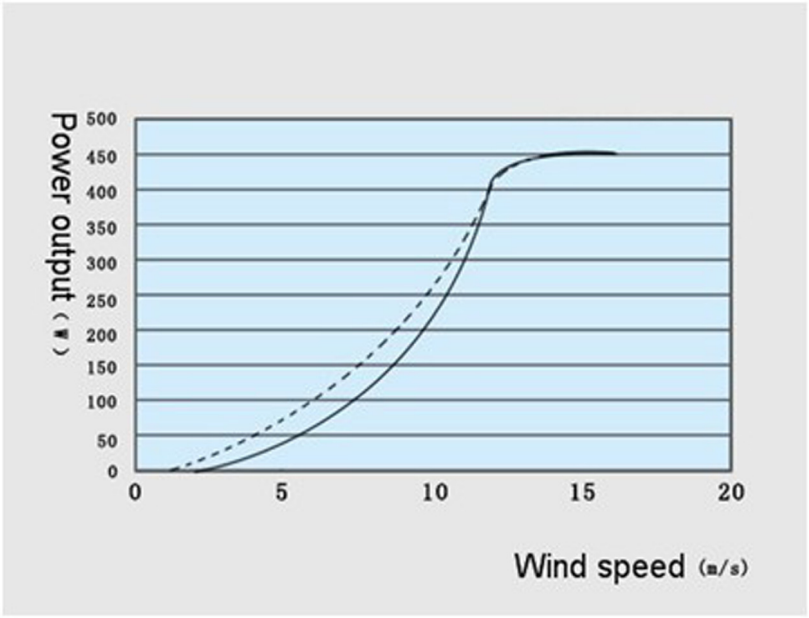

Fig. 15. Wind turbine's power curve.

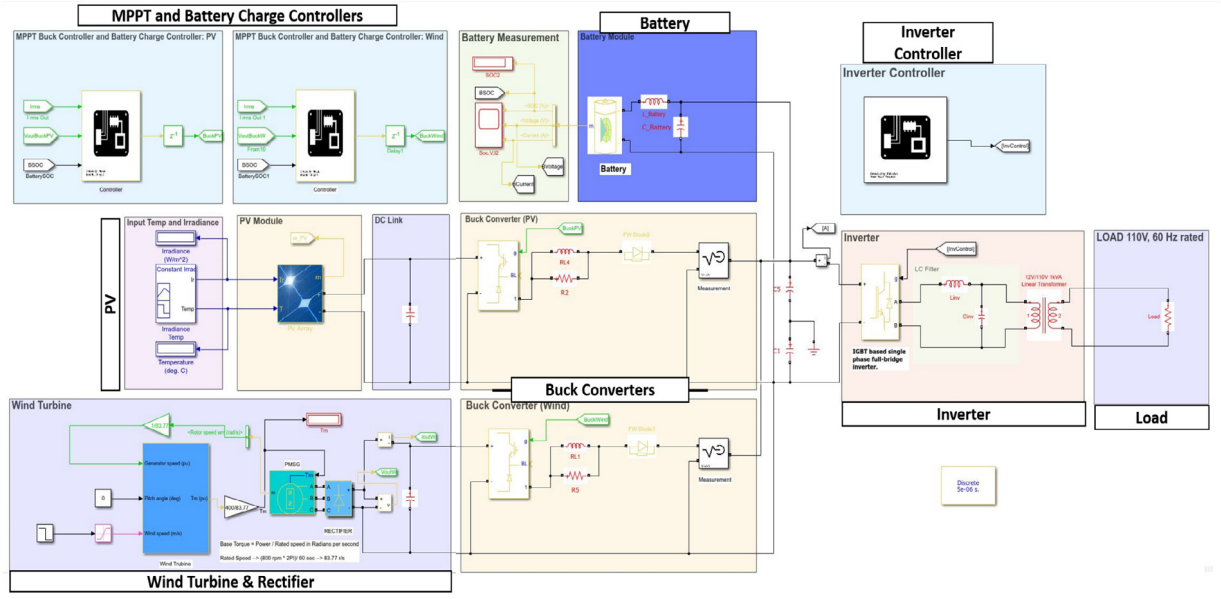

Fig. 16. HRES's MATLAB simulation model.

performance under varying weather conditions and the second showing the different modes of battery charging in changing system dynamics. The Total Harmonic Distortion (THD) of the proposed HRES has been calculated, as shown in Fig. 21. It is a very important factor of power quality related to grid regulations as well as the load's nominal frequency design. Even if the system is standalone, providing high power quality to the user is essential.

6.1. System's dynamics and performance under changing weather conditions scenario

This scenario has been implemented by varying the temperature, wind speed, and irradiance reported in Table 6.

Table 6
Scenario 1.

Time (s)	Temp °C	Wind speed m/s	Irradiance w/m^2
0	25	12.5	700
1.5	35	12.5	700
2	35	10	700
3	35	10	1000
4	35	10	1000

Fig. 22 shows the average power output form the proposed system by the various sources as well as the load power consumption. The system dynamics begin to stabilize around 0.5 s from the start of the operation, The average PV power between 1 s and 1.5 s is just below its MPPT which is 335 W at 700 w/m^2 – 25 °C. The wind turbine power at 12.5 m/s and 10 m/s can be

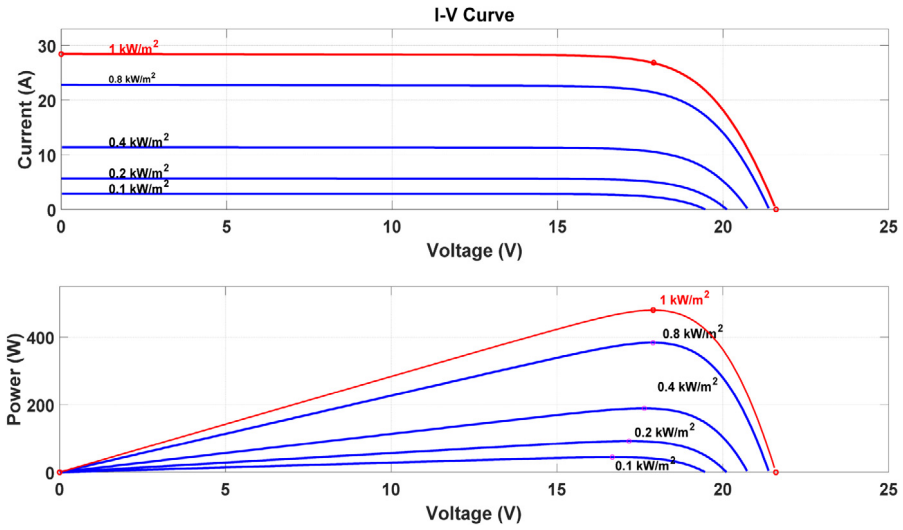

Fig. 17. PV module I–V and power curves under different solar irradiations.

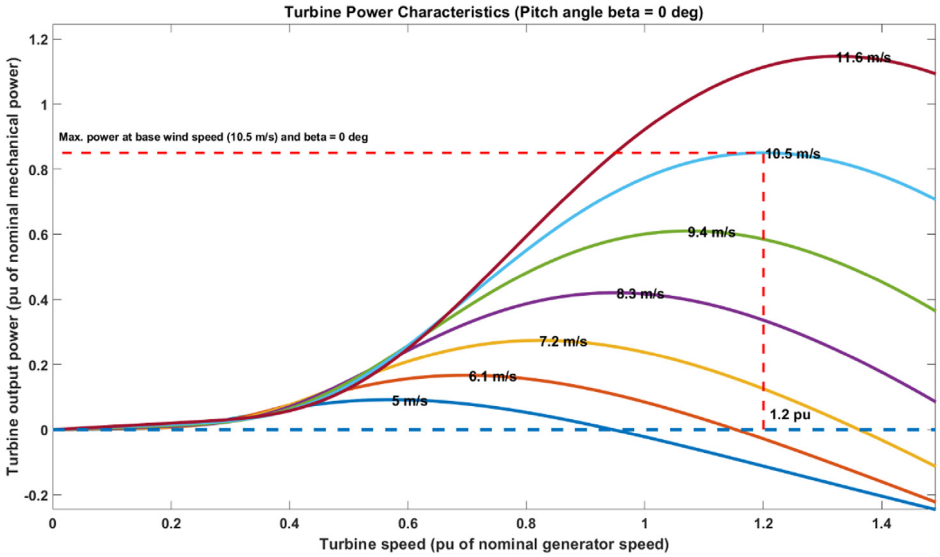

Fig. 18. Turbine power characteristics.

compared with Fig. 15, which is the real wind turbine's power characteristics, the model's performance is very close to its proposed power characteristics. This validates the models used for both PV and wind turbine. It can be observed that after 3.5 s at steady-state condition, the total power provided by the wind turbine, PV array, and the battery reaches 658 watts and the power loss is estimated at 58 watts, accounting for the inverter power loss (<10%) and other losses in the converters and components. It can also be observed from Fig. 22 that the control system can extract and track the maximum power from the PV as well as balancing the power from both the wind turbine and battery in response to the demand load requirements, under different irradiance, temperature, and wind speed. Whenever an environmental change or system dynamic occurs, the control system can quickly balance the power flow of the system. The battery can offset any drop of energy that the hybrid energy sources cannot sustain, within a short period of 2 to 4 s.

It can be depicted from Fig. 23 that the Total Harmonic Distortion is well under 1% in a steady-state condition, which is below the IEEE standard 514 limits (IEEE Recommended Practice and Requirements for Harmonic Control in Electric Power Systems, 2014), where it can converge to that under system changing dynamics, but can go above it during transient states. I can also be observed that the developed inverter control scheme stabilized the output voltage at the correct voltage range at 110 V RMS. Fig. 24(a) represents the output voltage and current waveforms. The clear sinewave form represents the low harmonics and high-power quality in the proposed system, as well as the 60 Hz, rated frequency. Fig. 24(b) shows the battery dynamics, where it was charging when there was enough renewable energy and compensating for the energy needed when the wind power decreased. Fig. 24(c) shows the buck converter controller's duty cycle, tracking the maximum power point, where the controller always converges to the required duty cycle whenever a change in the system state occurs. The observed oscillations in the duty cycle are related to the duty step specified in the perturb and observe the algorithm: the smaller the duty step size, the less steady-state oscillation, and slower divergence speed. Fig. 24(d) shows the PV array outputs, the fluctuations in voltage and current are due to the MPPT controller, and the DC bus bar fluctuations, where the PV power oscillates at the Maximum Power Point showing that the controller successfully tracked the

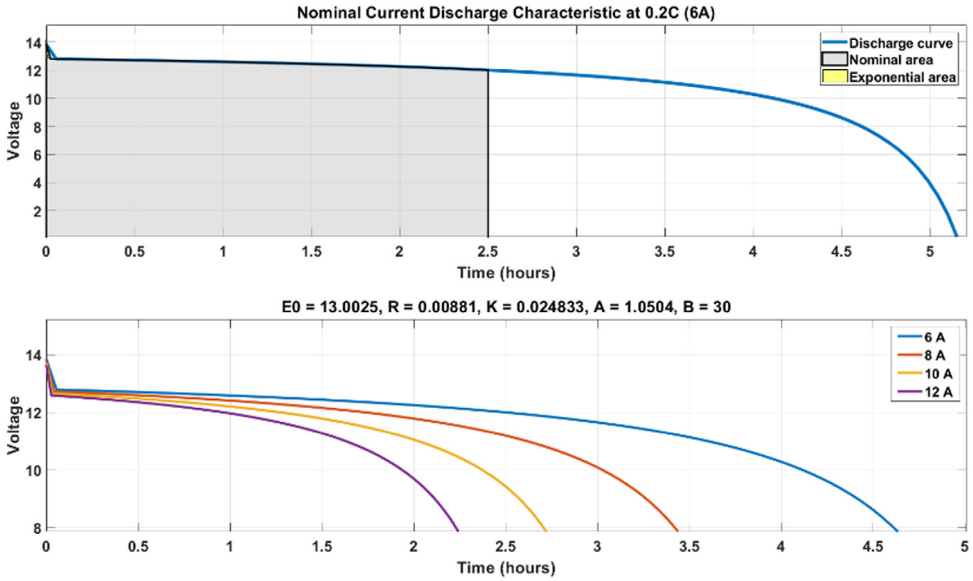

Fig. 19. Battery discharge characteristics.

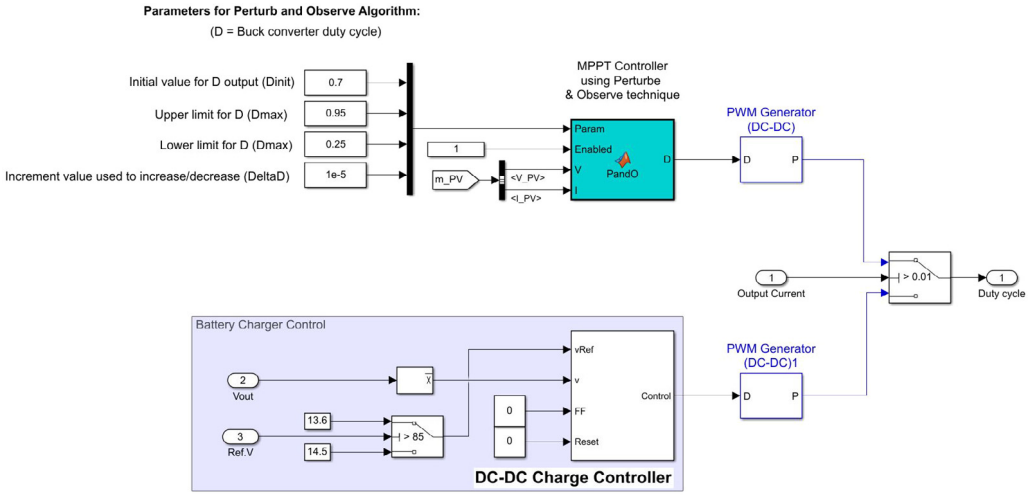

Fig. 20. MPPT and battery controller model.

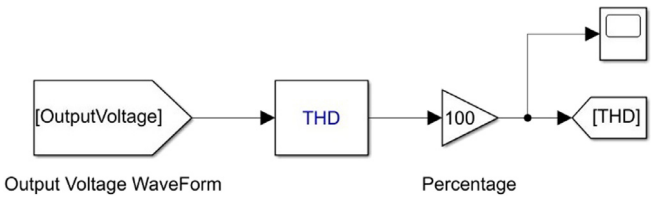

Fig. 21. Total harmonic distortion.

MPP. It can also be noticed that the increase in PV power is caused by an increase in the PV current output, where the PV voltage change remains under a smaller range.

6.2. Float & bulk charging scenario

This scenario has been set to test the battery charger's bulk and float modes. The Bulk mode fixes the DC bus bar's voltage at 14.5 V to enable faster charging when the SOC is below 85%, and there is no load connected. The float mode gives the battery a small charging current enough to keep it around the required maximum range as compared to the bulk mode, where the reference float voltage is set to 13.6 V. Table 7 shows the scenario for both float and bulk charging. For the Bulk scenario, the SOC of the battery starts at 79% and 86% for Float. The inverter and load have been disconnected to allow for more simulation time, as this scenario assumes no load. It can be observed from the bulk charging scenario in Fig. 25 that the charge controller can hold the voltage to the required 14.5 V range under changing weather conditions. It is clearly stated that the current is in the correct charging range according to the battery's manufacturer's recommendation (2–10 Amp) (V30-800 Deep Cycle, 0000), although it fluctuates above 10 A. The fluctuations in the voltage and current are due to the variation of the duty cycle of both buck converters. The controllers dissipate the extra power that the system produces by reducing the duty cycle of the buck converters.

Fig. 26 shows that the float mode can sustain the voltage in the correct range as suggested by the manufacturer (13.5–13.8 V) (V30-800 Deep Cycle, 0000). The buck converters dissipate the extra energy to prevent the battery from overcharging. The SOC of the battery is increasing far slower compared to the BulK mode. The higher the battery's voltage gets, as the battery charge

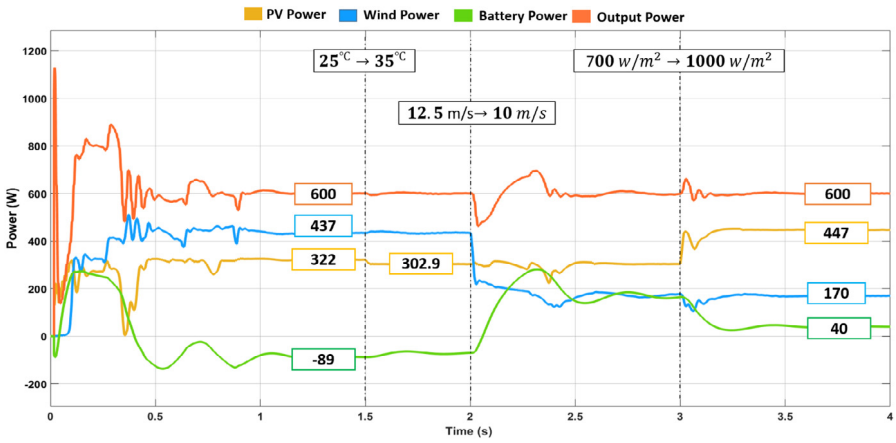

Fig. 22. Overall system dynamics.

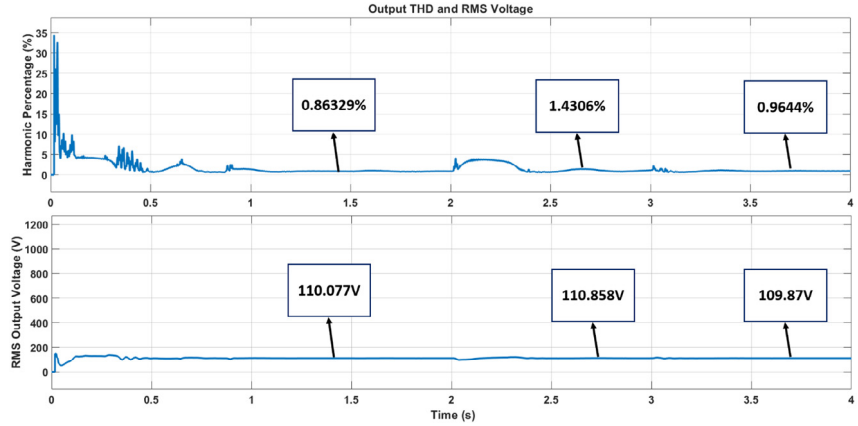

Fig. 23. Final voltage output RMS value and THD.

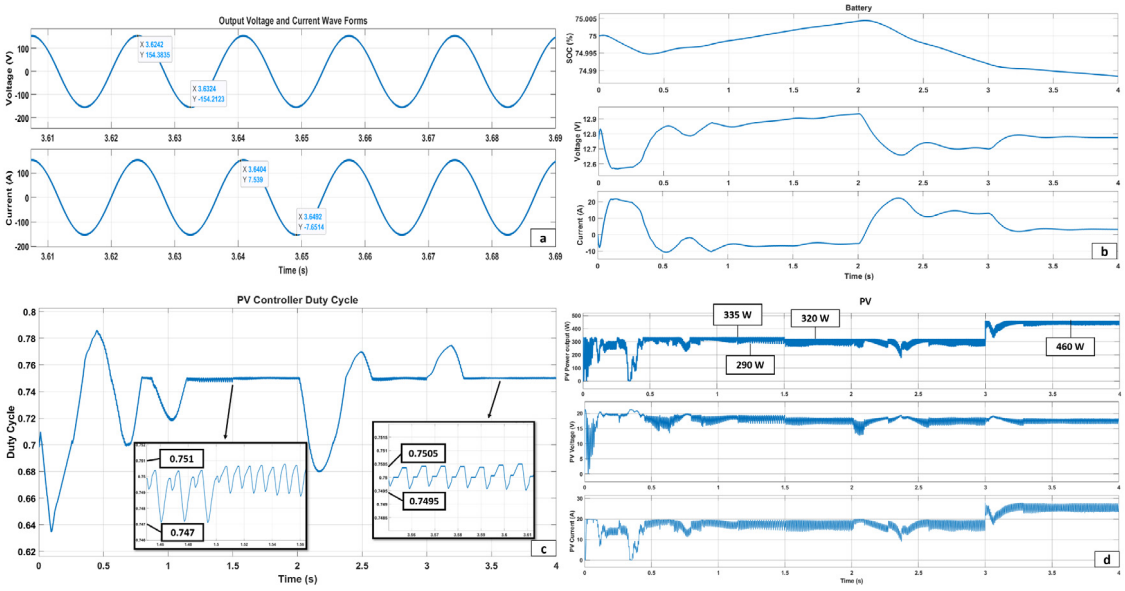

Fig. 24. (a) Output voltage and current waveform, (b) Battery SOC, voltage and current (c) MPPT duty cycle control, (d) PV power, voltage and current.

increases, the slower the charging rate gets. The fluctuations in float voltage set around 13.6 V are due to the fact the converters try only to allow a fraction of the renewable energy through and dissipate the rest in terms of heat energy.

The First Scenario demonstrated the validity of the model and control of the PV, wind, and Battery systems, as well as the converters and inverter. The output powers of the PV array and wind turbine were according to their proposed values shown in Section 4. The output voltage frequency, magnitude, and

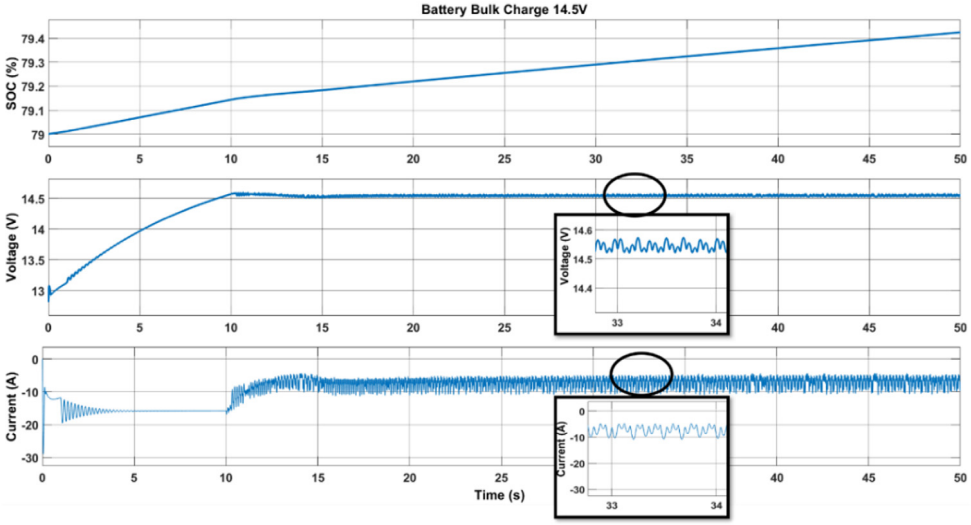

Fig. 25. Bulk charging scenario.

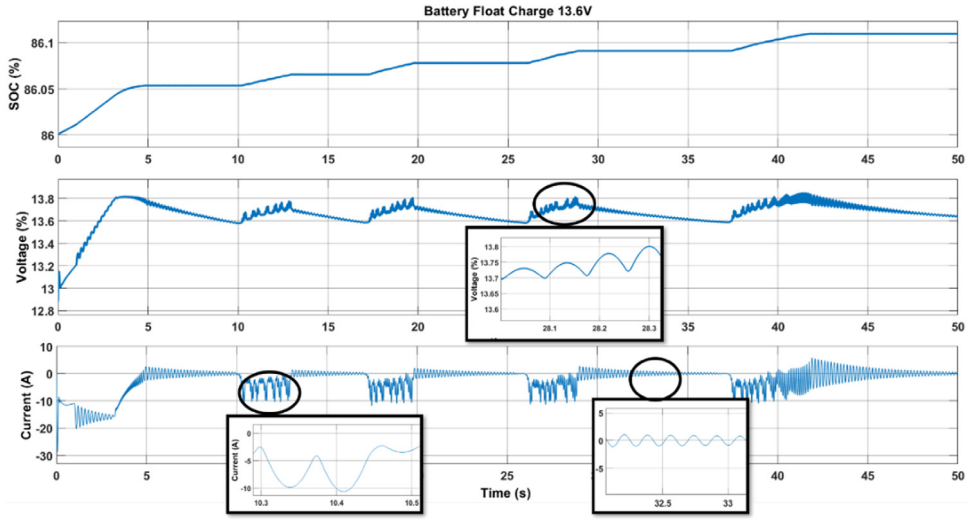

Fig. 26. Float charging scenario.

Table 7
Float & bulk charging scenario.

Time (s)	Temp °C	Wind speed m/s	Irradiance w/m^2
0	25	5	500
15	25	8	700

harmonic levels shown in Figs. 23 and 24(a) were as proposed in the inverter control scheme. The results also demonstrated the performance of the MPPT for the PV system, where it was able to reach the maximum power point at different irradiances and temperatures; however, there were oscillations and energy lost. The oscillation in the PV array output is heavily affected by the wind turbine's converter and the inverter connected to the system, as the continuous ON–OFF switching causes a lot of harmonics and affects the PV array output. It is essential when designing a standalone hybrid energy system to take the whole design into account. P&O might not lead to high oscillations if the PV array operated alone without the wind turbine. But in a hybrid system, the controllers should be more optimized and finely tuned to work in cohesion with each other. The second scenario demonstrated the proposed battery control schemes using the buck converter of both the wind turbine and PV array, were both float and buck voltages were achieved and sustained under changing weather conditions. It should be noted that the LC filter used at the battery, absorbs the current and voltage fluctuations of the battery during charging and discharging, and sustains the current in the required range. The wind turbine's simulation results showed good performance as it shares the same P&O MPPT as the PV array as well as the PI voltage control for the battery charging control, although it could be optimized further by more advanced control and MPPT tracking which was not taken into account in this research. The system should also be further optimized for extreme cases at very high and low renewable energy produced to ensure reliability and good performance for a wide range of cases. Finally, the filters used in the proposed design have achieved the purpose of reducing the harmonics in the system but can be further optimized to reduce cost.

7. Conclusion

In this paper, the control of a building integrated, standalone PV, and wind-turbine hybrid renewable power system with battery storage was presented. First, the main control layers were

discussed; P&O was used for MPPT for both the wind turbine and PV system, and PI control was used to control both the battery charging and inverter of the system. The system was modeled and simulated with MATLAB-Simulink, and the detailed components simulation and control implementation were discussed and presented thoroughly. The simulation results demonstrated the adequate performance of the proposed MPPT and battery charging control, as well as the inverter control implemented. Effective tracking of the MPP of the PV array was shown in the previous section, and the fluctuations seen in the PV output were discussed. Battery control was successfully achieved using the Buck converters of both the wind turbine and PV array, where the controllers were able to achieve the required charging voltages in float and bulk modes and dissipate the extra energy, without needing a specific converter and controller for the battery nor needing a dumb-load. The output power quality was achieved according to standard, and the correct voltage level was maintained using PI control of the Inverter. While other researches implement PV MPPT in a more simplified environment, it is important to show the performance of the MPPT under a detailed system simulation, especially in a hybrid system, where the MPPT and converter design should take into consideration the detailed system dynamics. The reduction and optimization of the filters used in this setup will also be taken into consideration for more price reduction while sustaining the required performance. Finally, optimizing the control parameters to be finely tuned for an extensive case of scenarios as well as different testing configurations and MPPT algorithms will be developed in future research.

However, the big challenge facing residential HRES like that we discussed in this paper is their economic viability and cost-effectiveness. Rather, cost-conscious policymakers often remain reluctant to invest financial resources in this area. Despite limited incentives provided by the local governments such as Feed-in-Tariff and J-Credit to compensate for the capital investments of a number of large-scale commercial and independent power producers, there are not any major regulatory efforts that have focused specifically on the promotion of the hybrid residential microgrids in Japan. Providing long-term policies and effective incentive strategies lead to the widespread deployment of residential microgrids in the whole country. The demonstration programs like that we discussed in this paper will help the government to set the long-term goals and an initial foundation for microgrid development in cities. Based on the detailed technical insights obtained from this study, the economic benefits of the proposed HRES for customers, utilities, and society can be evaluated, and then policies can be implemented to ensure the hybrid residential microgrid owner receives incentives or other support to monetize those benefits.

CRediT authorship contribution statement

Ayas Shaqour: Conceptualization, Methodology, Software, Writing - review & editing. **Hooman Farzaneh:** Conceptualization, Writing - review & editing, Supervision. **Yuichiro Yoshida:** Data curation, Investigation. **Tatsuya Hinokuma:** Data curation, Investigation.

Declaration of competing interest

The authors declare that they have no known competing financial interests or personal relationships that could have appeared to influence the work reported in this paper.

Acknowledgment

This research was supported by the Kurata grant of the Hitachi Global Foundation, Japan.

References

Ackermann, T., 2005. Wind Power in Power Systems. Wiley Online Library.

Afram, A., Janabi-Sharifi, F., Fung, A.S., Raahemifar, K., 2017. Artificial neural network (ANN) based model predictive control (MPC) and optimization of HVAC systems: A state of the art review and case study of a residential HVAC system. Energy Build. 141, 96–113. http://dx.doi.org/10.1016/J.ENBUILD.2017.02.012.

Akira, Yanagisawa, Aoshima, M., Arimoto, H., Yorita, Y., Kim, D.M., Ohira, T., Shibata, Y., Suehiroagus, S., Ito, K., 2018. Economic and energy outlook of Japan through FY2019. https://eneken.ieej.or.jp/data/8092.pdf.

Akram, M., Mezghani, D., Mami, A., 2017. Design and simulation of robust controllers for power electronic converters used in new energy architecture for a (PVG)/ (WTG) hybrid system. Int. J. Adv. Comput. Sci. Appl. 8, http://dx.doi.org/10.14569/ijacsa.2017.080531.

Alzahrani, A., Ferdowsi, M., Shamsi, P., Dagli, C.H., 2017. Modeling and simulation of microgrid. Procedia Comput. Sci. 114, 392–400. http://dx.doi.org/10.1016/j.procs.2017.09.053.

Athukorala, A.U.C.D., Jayasuriya, W.J.A., Ragulageethan, S., Sirimanna, M.P.G., Attalage, R.A., Perera, A.T.D., 2015. A techno-economic analysis for an integrated solar PV/T system with thermal and electrical storage — Case study. In: 2015 Moratuwa Eng. Res. Conf.. pp. 182–187. http://dx.doi.org/10.1109/MERCon.2015.7112342.

Bae, S., Kwasinski, A., 2012a. Dynamic modeling and operation strategy for a microgrid with wind and photovoltaic resources. IEEE Trans. Smart Grid 3, 1867–1876. http://dx.doi.org/10.1109/TSG.2012.2198498.

Bae, S., Kwasinski, A., 2012b. Dynamic modeling and operation strategy for a microgrid with wind and photovoltaic resources. IEEE Trans. Smart Grid 3, 1867–1876. http://dx.doi.org/10.1109/TSG.2012.2198498.

Barukčić, M., Hederić, Ž., Špoljarić, Ž., 2014. The estimation of I–V curves of PV panel using manufacturers' I–V curves and evolutionary strategy. Energy Convers. Manage. 88, 447–458. http://dx.doi.org/10.1016/J.ENCONMAN.2014.08.052.

Belabbas, B., Allaoui, T., Tadjine, M., Denai, M., 2019. Power management and control strategies for off-grid hybrid power systems with renewable energies and storage. Energy Syst. 10, 355–384. http://dx.doi.org/10.1007/s12667-017-0251-y.

Bendib, B., Belmili, H., Krim, F., 2015. A survey of the most used MPPT methods: Conventional and advanced algorithms applied for photovoltaic systems. Renew. Sustain. Energy Rev. 45, 637–648. http://dx.doi.org/10.1016/j.rser.2015.02.009.

Bhende, C.N., Mishra, S., Malla, S.G., 2011. Permanent magnet synchronous generator-based standalone wind energy supply system. IEEE Trans. Sustain. Energy 2, 361–373. http://dx.doi.org/10.1109/TSTE.2011.2159253.

Dahono, P.A., Purwadi, A., Qamaruzzaman, 1995. An LC filter design method for single-phase PWM inverters. In: Proc. 1995 Int. Conf. Power Electron. Drive Syst. PEDS 95, Vol. 2. pp. 571–576. http://dx.doi.org/10.1109/PEDS.1995.405006.

Dali, M., Belhadj, J., Roboam, X., 2010. Hybrid solar–wind system with battery storage operating in grid-connected and standalone mode: Control and energy management – Experimental investigation. Energy 35, 2587–2595. http://dx.doi.org/10.1016/J.ENERGY.2010.03.005.

Das, S., Akella, A.K., 2018. Power flow control of PV-wind-battery hybrid renewable energy systems for stand-alone application. Int. J. Renew. Energy Res. 8, 36–43.

De Brito, M.A.G., Galotto, L., Sampaio, L.P., De Azevedo Melo, G., Canesin, C.A., 2013. Evaluation of the main MPPT techniques for photovoltaic applications. IEEE Trans. Ind. Electron. 60, 1156–1167. http://dx.doi.org/10.1109/TIE.2012.2198036.

De Soto, W., Klein, S.A., Beckman, W.A., 2006. Improvement and validation of a model for photovoltaic array performance. Sol. Energy 80, 78–88. http://dx.doi.org/10.1016/J.SOLENER.2005.06.010.

Deshmukh, M.K., Deshmukh, S.S., 2008. Modeling of hybrid renewable energy systems. Renew. Sustain. Energy Rev. http://dx.doi.org/10.1016/j.rser.2006.07.011.

Di Piazza, M.C., La Tona, G., Luna, M., Di Piazza, A., 2017. A two-stage energy management system for smart buildings reducing the impact of demand uncertainty. Energy Build. 139, 1–9. http://dx.doi.org/10.1016/J.ENBUILD.2017.01.003.

Dulău, L.I., Abrudean, M., Bică, D., 2016. Smart grid economic dispatch. Procedia Technol. 22, 740–745. http://dx.doi.org/10.1016/j.protcy.2016.01.033.

El Wahid Hamza, K.A., Linda, H., Cherif, L., 2015. LCL filter design with passive damping for photovoltaic grid connected systems. In: 2015 6th Int. Renew. Energy Congr. IREC 2015. pp. 227–232. http://dx.doi.org/10.1109/IREC.2015.7110945.

Eleftheriadis, I.M., Anagnostopoulou, E.G., 2015. Identifying barriers in the diffusion of renewable energy sources. Energy Policy 80, 153–164. http://dx.doi.org/10.1016/j.enpol.2015.01.039.

Ellabban, O., Abu-Rub, H., Blaabjerg, F., 2014. Renewable energy resources: Current status, future prospects and their enabling technology. Renew. Sustain. Energy Rev. 39, 748–764. http://dx.doi.org/10.1016/J.RSER.2014.07.113.

Esteban, M., Portugal-Pereira, J., Mclellan, B.C., Bricker, J., Farzaneh, H., Djalilova, N., Ishihara, K.N., Takagi, H., Roeber, V., 2018. 100% renewable energy system in Japan: Smoothening and ancillary services. Appl. Energy 224, 698–707.

Et-torabi, K., Nassar-eddine, I., Obbadi, A., Errami, Y., Rmaily, R., Sahnoun, S., El fajri, A., Agunaou, M., 2017. Parameters estimation of the single and double diode photovoltaic models using a Gauss–Seidel algorithm and analytical method: A comparative study. Energy Convers. Manage. 148, 1041–1054. http://dx.doi.org/10.1016/j.enconman.2017.06.064.

Farzaneh, H., 2018. Devising a Clean Energy Strategy for Asian Cities. Springer.

Farzaneh, H., 2019a. Design of a hybrid renewable energy system based on supercritical water gasification of biomass for off-grid power supply in Fukushima. Energies 12, 2708.

Farzaneh, H., 2019b. Energy Systems Modeling: Principles and Applications. Springer.

Femia, N., Petrone, G., Spagnuolo, G., Vitelli, M., 2017. Power Electronics and Control Techniques for Maximum Energy Harvesting in Photovoltaic Systems. CRC press.

García, P., García, C.A., Fernández, L.M., Llorens, F., Jurado, F., 2014. ANFIS-based control of a grid-connected hybrid system integrating renewable energies, hydrogen and batteries. IEEE Trans. Ind. Inform. 10, 1107–1117. http://dx.doi.org/10.1109/TII.2013.2290069.

Gong, J., Kostro, A., Motamed, A., Schueler, A., 2016. Potential advantages of a multifunctional complex fenestration system with embedded micro-mirrors in daylighting. Sol. Energy 139, 412–425. http://dx.doi.org/10.1016/J.SOLENER.2016.10.012.

Haroun, R., El Aroudi, A., Cid-Pastor, A., Garíca, G., Olalla, C., Martínez-Salamero, L., 2015. Impedance matching in photovoltaic systems using cascaded boost converters and sliding-mode control. IEEE Trans. Power Electron. 30, 3185–3199. http://dx.doi.org/10.1109/TPEL.2014.2339134.

Hart Danial, W., 2010. Power_Electronics.

Heier, S., Waddington, R., 1998. Grid Integration of Wind Energy Conversion Systems. Wiley, https://books.google.co.jp/books?id=C5dz4hlvF0EC.

Höök, M., Tang, X., 2013. Depletion of fossil fuels and anthropogenic climate change—A review. Energy Policy 52, 797–809. http://dx.doi.org/10.1016/J.ENPOL.2012.10.046.

Husain, A.T.M.A., 2013. Modeling of a standalone wind-PV hybrid generation system using MATLAB/SIMULINK and its performance analysis. Ijser. 4, 1805–1811. http://dx.doi.org/10.3969/j.

Hwas, A., Katebi, R., 2012. Wind turbine control using PI pitch angle controller. IFAC Proc. 2, 241–246.

IEEE Recommended Practice and Requirements for Harmonic Control in Electric Power Systems, in: IEEE Std 519-2014 (Revision of IEEE Std 519-1992), pp. 1–29, 11 June 2014, https://doi.org/10.1109/IEEESTD.2014.6826459.

Jordehi, A.R., 2016. Maximum power point tracking in photovoltaic (PV) systems: A review of different approaches. Renew. Sustain. Energy Rev. 65, 1127–1138. http://dx.doi.org/10.1016/j.rser.2016.07.053.

Kalantar, M., Mousavi, G.S.M., 2010. Dynamic behavior of a stand-alone hybrid power generation system of wind turbine, microturbine, solar array and battery storage. Appl. Energy 87, 3051–3064. http://dx.doi.org/10.1016/j.apenergy.2010.02.019.

Kartite, J., Cherkaoui, M., 2019. Study of the different structures of hybrid systems in renewable energies: A review. Energy Procedia 157, 323–330. http://dx.doi.org/10.1016/j.egypro.2018.11.197.

Kaygusuz, A., Keles, C., Alagoz, B.B., Karabiber, A., 2013. Renewable energy integration for smart sites. Energy Build. 64, 456–462. http://dx.doi.org/10.1016/J.ENBUILD.2013.05.031.

Kim, S.K., Jeon, J.H., Cho, C.H., Ahn, J.B., Kwon, S.H., 2008a. Dynamic modeling and control of a grid-connected hybrid generation system with versatile power transfer. IEEE Trans. Ind. Electron. 55, 1677–1688. http://dx.doi.org/10.1109/TIE.2007.907662.

Kim, H., Sul, S.K., 2011. A novel filter design for output LC filters of PWM inverters. J. Power Electron. 11, 74–81. http://dx.doi.org/10.6113/JPE.2011.11.1.074.

Kim, H., Yu, T., Choi, S., 2008b. Indirect current control algorithm for utility interactive inverters in distributed generation systems. IEEE Trans. Power Electron. 23, 1342–1347. http://dx.doi.org/10.1109/TPEL.2008.920879.

Ko, H.S., 2014. Modeling and control of PMSG-based variable-speed wind turbine. Adv. Ind. Control 80, 3–21. http://dx.doi.org/10.1007/978-3-319-08413-8_1.

Krause, P.C., Wasynczuk, O., Sudhoff, S.D., Pekarek, S., 2002. Analysis of Electric Machinery and Drive Systems. Wiley Online Library.

Kumar, K., Ramesh Babu, N., Prabhu, K.R., 2017. Design and analysis of an integrated Cuk-SEPIC converter with MPPT for standalone wind/PV hybrid system. Int. J. Renew. Energy Res. 7, 96–106.

Le Guen, M., Mosca, L., Perera, A.T.D., Coccolo, S., Mohajeri, N., Scartezzini, J.-L., 2018. Improving the energy sustainability of a Swiss village through building renovation and renewable energy integration. Energy Build. 158, 906–923. http://dx.doi.org/10.1016/J.ENBUILD.2017.10.057.

Li, Q.S., Shu, Z.R., Chen, F.B., 2016. Performance assessment of tall building-integrated wind turbines for power generation. Appl. Energy 165, 777–788. http://dx.doi.org/10.1016/J.APENERGY.2015.12.114.

Ma, L., Liu, N., Wang, L., Zhang, J., Lei, J., Zeng, Z., Wang, C., Cheng, M., 2016. Multi-party energy management for smart building cluster with PV systems using automatic demand response. Energy Build. 121, 11–21. http://dx.doi.org/10.1016/J.ENBUILD.2016.03.072.

Mangu, B., Akshatha, S., Suryanarayana, D., Fernandes, B.G., 2016. Grid-connected PV-wind-battery-based multi-input transformer-coupled bidirectional DC-DC converter for household applications. IEEE J. Emerg. Sel. Top. Power Electron. 4, 1086–1095. http://dx.doi.org/10.1109/JESTPE.2016.2544789.

Martinello, D., Carati, E.G., da Costa, J.P., Cardoso, R., Stein, C.M.O., 2016. Emulation of wind turbines. In: Wind Turbines - Des. Control Appl.. InTech, p. 13. http://dx.doi.org/10.5772/63448.

McLellan, B.C., Zhang, Q., Utama, N.A., Farzaneh, H., Ishihara, K.N., 2013. Analysis of Japan's post-Fukushima energy strategy. Energy Strategy Rev. 2, 190–198.

METI/ANRE, 2018. Total Energy Statistics. https://www.enecho.meti.go.jp/statistics/total_energy/results.html#headline2.

Mohan, N., Undeland, T.M., Robbins, W.P., 2003. Power Electronics: Converters, Applications, and Design. John Wiley & Sons, https://books.google.co.jp/books?id=ToYoAQAAMAAJ.

Morais, H., Kádár, P., Faria, P., Vale, Z.A., Khodr, H.M., 2010. Optimal scheduling of a renewable micro-grid in an isolated load area using mixed-integer linear programming. Renew. Energy 35, 151–156. http://dx.doi.org/10.1016/j.renene.2009.02.031.

Papantoniou, S., Kolokotsa, D., Kalaitzakis, K., 2015. Building optimization and control algorithms implemented in existing BEMS using a web based energy management and control system. Energy Build. 98, 45–55. http://dx.doi.org/10.1016/J.ENBUILD.2014.10.083.

Pérez-Lombard, L., Ortiz, J., Pout, C., 2008. A review on buildings energy consumption information. Energy Build. 40, 394–398. http://dx.doi.org/10.1016/j.enbuild.2007.03.007.

Rocha, P., Siddiqui, A., Stadler, M., 2015. Improving energy efficiency via smart building energy management systems: A comparison with policy measures. Energy Build. 88, 203–213. http://dx.doi.org/10.1016/J.ENBUILD.2014.11.077.

Rouholamini, M., Mohammadian, M., 2015. Energy management of a grid-tied residential-scale hybrid renewable generation system incorporating fuel cell and electrolyzer. Energy Build. 102, 406–416. http://dx.doi.org/10.1016/j.enbuild.2015.05.046.

Saravanan, S., Ramesh Babu, N., 2016. Maximum power point tracking algorithms for photovoltaic system - A review. Renew. Sustain. Energy Rev. 57, 192–204. http://dx.doi.org/10.1016/j.rser.2015.12.105.

Sassi, A., Zaidi, N., Nasri, O., Ben Hadj Slama, J., 2017. Energy management of PV/wind/battery hybrid energy system based on batteries utilization optimization. In: Int. Conf. Green Energy Convers. Syst. GECS 2017. http://dx.doi.org/10.1109/GECS.2017.8066133.

Sera, D., Mathe, L., Kerekes, T., Spataru, S.V., Teodorescu, R., 2013. On the perturb-and-observe and incremental conductance mppt methods for PV systems. IEEE J. Photovolt. 3, 1070–1078. http://dx.doi.org/10.1109/JPHOTOV.2013.2261118.

Shongwe, S., Hanif, M., 2015. Comparative analysis of different single-diode PV modeling methods. IEEE J. Photovolt. 5, 938–946. http://dx.doi.org/10.1109/JPHOTOV.2015.2395137.

Sikder, P.S., Pal, N., 2019. Modeling of an intelligent battery controller for standalone solar-wind hybrid distributed generation system. J. King Saud Univ. - Eng. Sci. http://dx.doi.org/10.1016/J.JKSUES.2019.02.002.

Takatsu, N., Farzaneh, H., 2020. Techno-economic analysis of a novel hydrogen-based hybrid renewable energy system for both grid-tied and off-grid power supply in japan: the case of fukushima prefecture. Appl. Sci. 10, 4061.

Tan, R., 2020. Pure Sine Wave Off Grid Inverter Demo. https://https//www.mathworks.com/matlabcentral/fileexchange/56506-pure-sine-wave-off-grid-inverter-demo.

T.I. Incorporated, 2000. Texas Instruments Incorporated - Second-Stage LC Filter Design. Texas Instruments Inc., pp. 8–10, http://www.ti.com/lit/an/slaa701a/slaa701a.pdf.

Tremblay, O., Dessaint, L.A., 2009. Experimental validation of a battery dynamic model for EV applications. World Electr. Veh. J. 3, 289–298.

V30-800 Deep Cycle, High performance AGM Battery. (n.d.). https://www.vmaxtanks.com/V30-800-Deep-Cycle-High-performance-AGM-Battery-_p_46.html.

Valenciaga, F., Puleston, P.F., 2005. Supervisor control for a stand-alone hybrid generation system using wind and photovoltaic energy. IEEE Trans. Energy Convers. 20, 398–405. http://dx.doi.org/10.1109/TEC.2005.845524.

Walker, S.L., 2011. Building mounted wind turbines and their suitability for the urban scale—A review of methods of estimating urban wind resource. Energy Build. 43, 1852–1862. http://dx.doi.org/10.1016/J.ENBUILD.2011.03.032.

Wang, C., Nehrir, M.H., 2008. Power management of a stand-alone wind/photovoltaic/fuel cell energy system. IEEE Trans. Energy Convers. 23, 957–967. http://dx.doi.org/10.1109/TEC.2007.914200.

Yoshida, Y., Farzaneh, H., 2020. Optimal design of a stand-alone residential hybrid microgrid system for enhancing renewable energy deployment in Japan. Energies 13, 1737.